Reflective tomography solved by the inverse Radon transform

Gaël Rigaud, Jean-Baptiste Bellet, Gérard Berginc, Ion Berechet, Stefan Berechet

Reflective tomography solved by the inverse Radon transform

Gaël Rigaud*, Jean-Baptiste Bellet*, Gérard Berginc†,
Ion Berechet‡, and Stefan Berechet‡

* *Université de Lorraine, Institut Elie Cartan de Lorraine, UMR 7502, Metz, France.*
† *THALES Optronique SA, 2, 78995 Elancourt, France.*
‡ *Société SISPIA, 94300 Vincennes, France.*

September 29, 2015

Abstract

This paper is concerned with imaging a 3D scene from a set of 2D laser images of backscattered intensity. The interaction between an electromagnetic wave and a medium can be understood and modeled in different ways. In the context considered here, the interaction results in a 3D projection of the scene. After inspection in this projection, the reflection data appear as a sum in 3D of local sinograms with severely limited angle view. Therefore, the approach proposed here consists in considering reflection data as an incomplete data set of Radon-kind used in conventional Computerized Tomography (CT). Under this assumption, the use of the reconstruction techniques, such as the well-known filtered backprojection (FBP), provides a 3D-surface reconstruction of the scene from reflective data. Such 3D reconstructions are performed with short computation times. Simulation results using real data in laser tomography attest of the strength and of the relevancy of such an approach.

1 Introduction

Imaging is an area of research that, because of its vital importance and sometimes the wide variety of applications, focused a tremendous amount of work since the early 1970s. The appearance and the development of the first X-ray scanners, followed a few years later by the breakthrough of magnetic resonance imaging, have made the use of these devices essential for the proper functioning of our societies. The basis of imaging lies on the understanding and the modeling of the interactions between an electromagnetic wave and a sought object. Then, according to the kind of electromagnetic waves, different concepts has emerged : X-rays in CT [10] or radiography, magnetic fields in MRI, ultrasounds in US imaging...

In this paper, we are focused on visible and infrared spectrums. We assume that a laser source emits in the visible or near-infrared band (from 500 nm to 2200 nm) and that the pixels of a focal plane area collect the backscattered intensity; the phase of the backscattered wave is not measured. The acquisition is assumed to be monostatic: the 2D array of receivers is close to the source. The scene is finally illuminated for different positions of the acquisition device, and thus we get a collection of 2D images, for several angles of view. These images need to be treated to get a 3D reconstruction of the original scene.

The reconstruction of a 3D scene by combining several intensity images recalls Computerized Tomography from X-Ray transmission tomography. Thus several authors have already proposed to extend the use of X-Ray algorithms to visible and near-infrared spectrum [1, 2]; in particular the FDK algorithm [3] is at the heart of a reconstruction method for the problem which is mentionned above [4–8]. Since backscattering is a strong component of the considered laser images, such an imaging method is sometimes called *reflective tomography*, to be contrasted with transmission tomography.

A full mathematical description of reflective tomography is still needed. So we start by studying some canonical case of reflection data. We identify the support of reflection data with the support of Radon data; we also express reflection data as incomplete Radon-kind data. This motivates the use of transmission inversion methods such as filtered back-projection (FBP) [9]. Then we present Laser Imagery: we apply the FDK algorithm on realistic laser data. We present some visualization of the 3D reconstructions, by thresholding. The results show the relevancy of this approach.

This paper is organized as follows. We first recall the basis of the classical Radon and X-ray transforms used in medical imaging as well as the FBP algorithm and the concept of the cone-beam computed tomography. Then, we present the working principle of the modality in reflection imaging that we propose to study. Simulation results are obtained on synthetic data. Finally, we consider a real laser imaging system. The use of a classical FBP or FDK algorithm on such data appears relevant and efficient for recovering 3D scene from a 2D images set. A conclusion ends the paper.

2 Recall on some Radon transforms

2.1 The 2D Radon transform

This particular case was rediscovered and studied by Cormack and we will focus on it because of its interest in tomography. As we need to give coordinates on the unit sphere S^1, we denote the unit vector in direction $\varphi \in [0, 2\pi]$ as Θ and its orthogonal as $\Theta^\perp$:

$$\Theta = (\cos\varphi, \sin\varphi), \quad \Theta^\perp = (-\sin\varphi, \cos\varphi). \tag{1}$$

We define

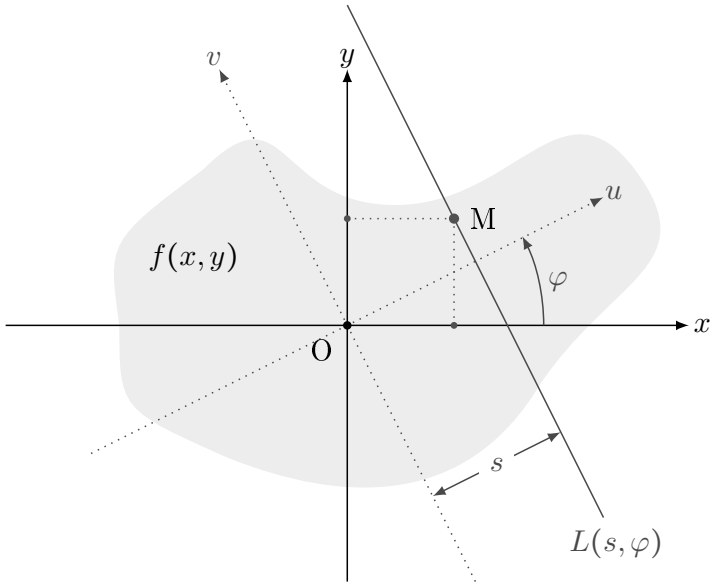

Figure 1: Geometric setup of the integration along a straight line

$$L(s,\varphi) = \{x \in \mathbb{R}^2 | x \cdot \Theta(\varphi) = s\} \tag{2}$$

to be the line perpendicular to $\Theta(\varphi)$ and s directed units from the origin. The Radon transform of a function $f \in \mathcal{L}^2(\mathbb{R}^2)$ is given by

$$\mathcal{R}f(s,\varphi) = \int_{(x,y)\in L_{s,\varphi}} f(x,y)\ dl = \int_{\mathbb{R}} f(s\Theta + t\Theta^{\perp})dt, \tag{3}$$

and is continuous. This integral operator represents the projection of a given function over hyperplanes parametrized by the pair $(s,\Theta) \in \mathbb{R} \times S^1$. J. Radon introduced this transform in 1917 for pure mathematical reason. The adjoint Radon transform of a function $g \in \mathcal{L}^2(\mathbb{R} \times S^1)$ is then deduced to

$$\left(\mathcal{R}^{\star} g\right)(x) = \int_{S^1} g(x \cdot \Theta, \Theta) d\Theta. \tag{4}$$

This operator can be interpreted as the spreading of the value of $g(s,\Theta)$ over the hyperplane defined by $s = x \cdot \Theta$. This explains why this operator is often called the Back-projection operator.

2.2 The X-ray transform

The 3-dimensional X-ray transform $\mathcal{P}$ maps a function on $\mathbb{R}^3$ into the set of its line integrals. More especially, for $\Theta \in S$ and $x \in \mathbb{R}^3$,

$$\mathcal{P}f(\Theta, x) = \int_{\mathbb{R}} f(x + t\Theta)dt \tag{5}$$

is the integral of $f \in \mathcal{L}^2(\mathbb{R}^3)$ over the straight line through x with direction Θ. We can notice the 2-dimensional X-ray transform matches with the standard 2-dimensional Radon transform. Its inversion formula is given using the Riesz potential $\mathcal{I}^{-1}$ and the backprojection operator $\mathcal{P}^*$,

$$f = (2\pi)^{-2}\mathcal{P}^*\mathcal{I}^{-1}g, \qquad g = \mathcal{P}f. \tag{6}$$

The above expression is classically called a filtered backprojection since the computation of the Riesz potential is performed in Fourier space using an apodized ramp filter, see [9, 10].

2.3 Cone-beam computed tomography

Cone beam computed tomography (CBCT) is a medical imaging technique working by transmission where the X-rays form a cone. The use of CBCT has increased in the last decades in treatment planning and diagnosis, and has been widely studied, [11]. In particular, the well-known Grangeat's algorithm enables to change the cone-beam geometry data in classical parallel geometry data [9] which are easily inverted [12, 13]. An approximation of this change of spaces leads to a reconstruction technique called the FDK algorithm [3, 14].

Due to the strong connection between the cone-beam and parallel geometries, we will consider in our study only the parallel one for the sake of simplicity. Then, in the next section we present the working principle of reflection imaging for the 2D case. The 3D case is extended due to these relations.

3 Reflective tomography

3.1 Working principle

We now present the essence of this work. We consider an acquisition system similar to a CBCT except that the source and the flat detector (a detectors grid) are located from the same side of the object, see Fig. 2. Whereas X-rays illuminate and propagate into the object in CBCT, here the source emits from visible to infrared waves. This changes completely the modality since with the considered frequency range, the emitted waves are mainly scattered instead of being transmitted. Therefore, the use of reflection properties of the electromagnetic waves on the sought object will bring us information about the apparent 3D surface and not on the whole volume.

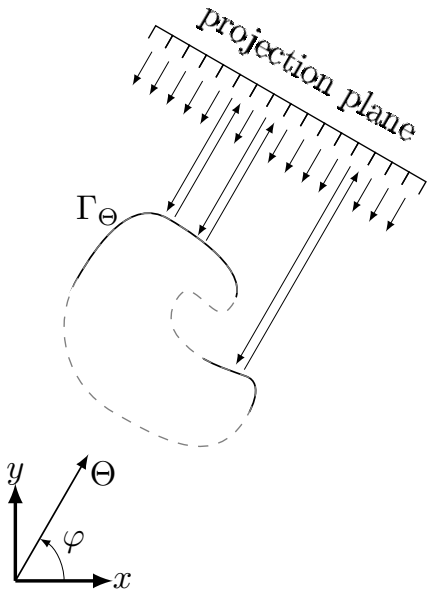

Figure 2: Setup for our reflection modality in 2D with a parallel geometry.

From a phenomenological point of view, the electromagnetic field diffused by a rough surface will be more or less specular or diffuse depending on the roughness state of the diffuse surface [15–20]. Fig.4 exhibits the contributions of the two contributors depending on the roughness state of the surface. For a perfect plane (a) the diffused field is completely determinist and its phase is well knows. When the roughness increases (b) an incoherent contributor appears which phase is totally random. For a very strong roughness (c) only the diffused contributor remains. The coherent component of the electromagnetic scattered field is a deterministic value, the incoherent component is a stochastic one with a null mean value.Therefore, the electromagnetic field backscattered by a randomly rough surface, which a random variable depending on the stochastic process of the representation of the object surface, is given by the first (coherent component) and second (diffuse or incoherent component) moments of the field. Most of natural surfaces or manufactured materials observed in an optronic scene have a strong diffused contributor and even if specular reflections can occur, they are linked to very tight observation angles.

As electromagnetic wave propagating in a given medium, measured data will suffer from an attenuation effect. Other phenomena while propagating through atmosphere as scintillation, beam wandering are taken into account. Below, for our mathematical development we consider that such factors can be compensated or neglected.

In the case of the visible spectrum, the assumption is often to consider a lambertian modeling: it simplifies the analysis. We will see in more details this

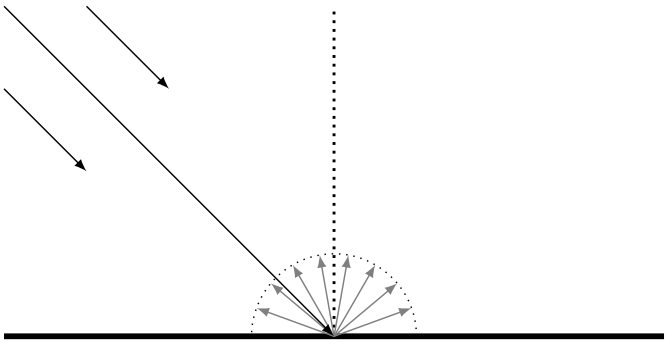

Figure 3: Reflection on a lambertian surface.

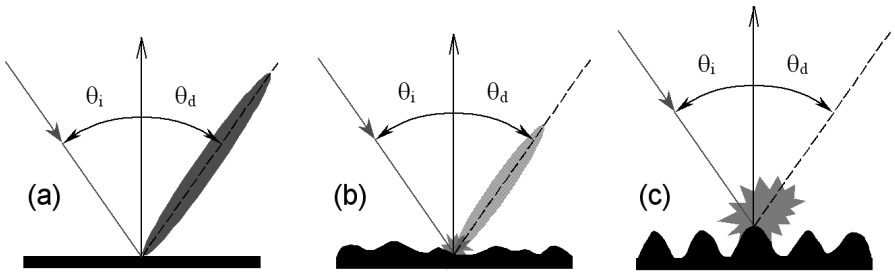

Figure 4: Representation of the specular and diffuse contributors depending on the surface state

case in the next section.

3.2 Lambertian surface

When the surfaces are randomly rough, with rough patches larger than the wavelength of the incident radiation, we can consider for a Lambertian interface that the the electromagnetic wave is uniformly scattered in any direction. It is classical to consider a lambertian surface [21] in this kind of stereovision for instance. In this case, the intensity of the reflected radiation is independant of the direction, see Fig. 3.

We now consider a backscattered imaging system. The data acquisition is assumed parallel and the object surface is taken lambertian. We take the same point for the source and detection point, see Fig. 2. Then for a given position of the source/detector grid (and so for $\Theta \in S^1$), measurement will correspond to the projection of the observed surface. We denote by Γ_Θ the observed surface

in the direction $\Theta = (\cos\varphi, \sin\varphi)$.

In this context, one can define the projections $I(p,\Theta)$ on the line $L(p,\Theta)$ in the sense of the reflection as

$$g_L(p,\Theta) = f(x = \Gamma_\Theta \cap L(p,\Theta)) \tag{7}$$

where the function $f > 0$ stands for a reflectivity characteristic function of the illuminated surface and $p \in \mathbb{R}$ denotes the radial position of the detector. Due to the definition of Γ_Θ, we have unicity of the intersection when $\Gamma_\Theta \cap L(p,\Theta) \neq \emptyset$. It can be noticed that the measurements are *formally* related to a special Radon transform

$$g_L(p,\Theta) = \mathcal{R}\left(f \times \delta_{\Gamma_\Theta}\right)(p,\Theta) \tag{8}$$

where δ_{Γ_Θ} characterizes the visible contour Γ_Θ. Of course, this data are not in the range of the Radon transform because of the dependancy to Θ of the function itself and therefore cannot be stricly inverted. However it is interesting to notice that for a sufficiently regular surface, a given point of the surface will be observed and then measured on a given angular range. In this context, the problem of image reconstruction can be understood as an incomplete data issue [22].

Another important point is the support. Indeed, the data g_L describes the same support than the Radon transform of the sought object/contours. Equivalently this means that g_L and $\mathcal{R}f$ are null at the same set of points. Then, a first reconstruction of the object is possible using the support theorem, see [23]. This can reconstruct the convex envelope of the object, and it can be useful to clean the noise outside the convex hull.

We see below that the application of a classical filtered back-projection algorithm on our data g_L can be sufficient to reconstruct the contours of our object. Since we consider a data set of size sufficiently large (larger than the number of pixels of the image), we have more data points than contours points to reconstruct. This can explain the quality of the reconstruction that we obtain in spite of the incompleteness issue.

3.3 Simulation results on synthethic data

We now present simulation results on synthetic data. We consider the contour which is depicted in Fig. 5 as the original image in the setup. The image is defined on a 256x256 grid. At every pixel of the contour, the function f is a random number (uniform law between 0.1 and 1). This canonical object enables to observe how the method deals with non-convexity, which generates occultations.

We first have to compute the reflection data of these contours, by following eq. (7). We consider an angular vector $\varphi = \{\frac{\pi}{N}, \frac{2\pi}{N}, ..., \pi\}$ where $N = 256$. The detector parameter is p is defined from $-\frac{N}{\sqrt{2}}$ to $\frac{N}{\sqrt{2}}$ with $\Delta p = 1$ the sampling step. Fig. 6 shows the data that we obtained from Fig. 5. It is interesting to compare this data with the classical Radon transform of the original contours, $\mathcal{R}f$, which is displayed in Fig. 7, especially in terms of support; see Fig. 8,

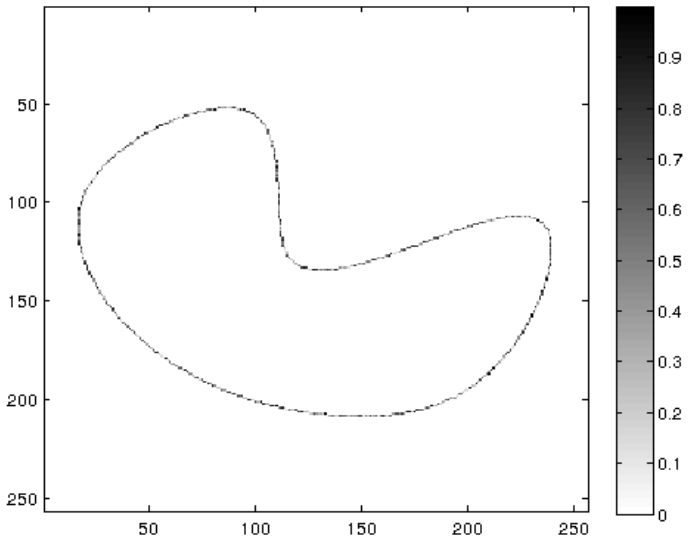

Figure 5: Original synthetic contours

which is a binarisation of the reflection data. As expected, both data have the same support which means the same null set. The integral effect of $\mathcal{R}$ leads to continuous data set (Fig. 7) whereas for our reflection modality (Fig. 6), data are composed of incomplete and distinguishable point spread function (the impulse response which is a cosine function) involved by each piece of the contours.

To reconstruct the function f, we apply the filtered back-projection algorithm which can be written as

$$f(x) = \frac{1}{4\pi}\mathcal{R}^*\mathcal{H}\frac{\partial}{\partial p}g(p,\varphi). \tag{9}$$

We use the standard way performing the Hilbert transform, $\mathcal{H}$, in Fourier space and multiplying by an apodized ramp filter (here Hann function is used as apodization). Then we have to apply the back-projection operator $\mathcal{R}^*$ on the filtered data g^* defined as

$$g^*(p,\varphi) = \mathcal{F}^{-1}\left\{|\nu| \cdot \mathcal{F}\left\{g(p,\varphi)\right\}\right\}, \tag{10}$$

where $\mathcal{F}$ (resp. $\mathcal{F}^{-1}$) stands for the 1D-Fourier transform (resp. the inverse 1D-Fourier transform). Its computation is performed by a Fast Fourier transform (FFT). Because of frequency unstability and cut-off we have to apodize the

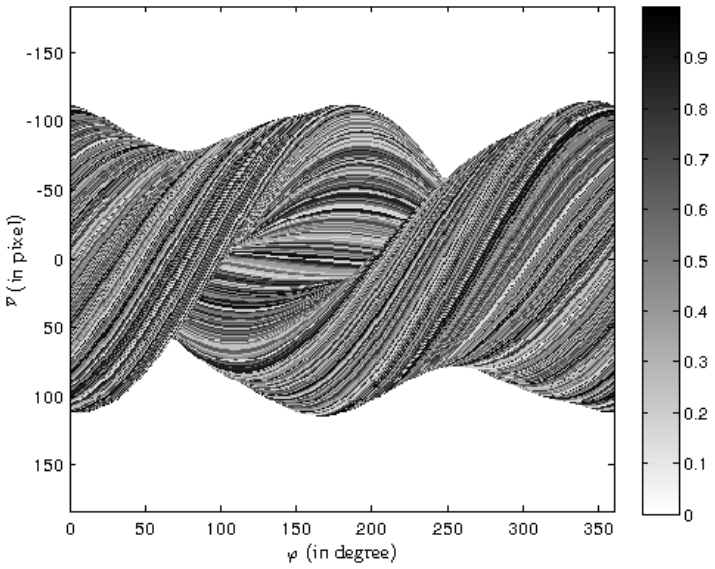

Figure 6: Reflection data from Fig. 5.

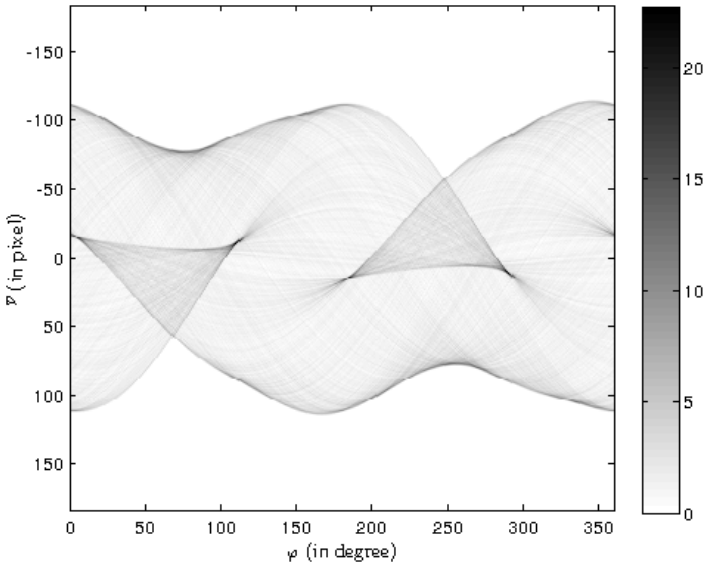

Figure 7: Radon data from Fig. 7.

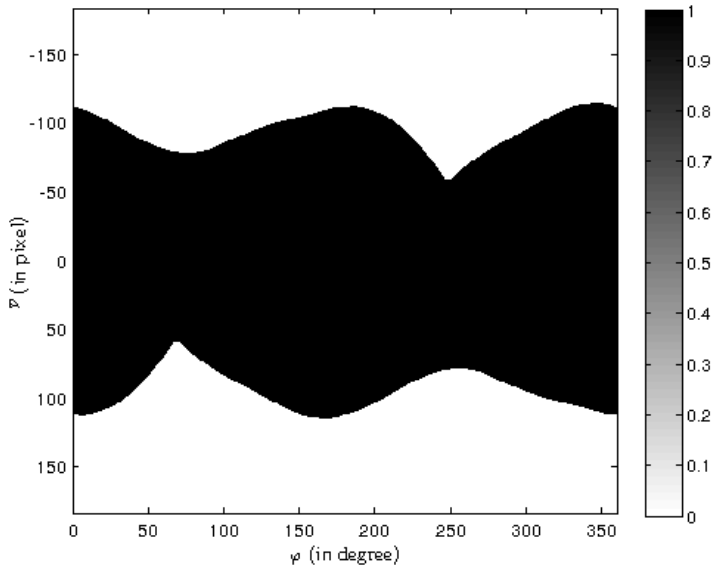

Figure 8: Support of Fig. 6 (and Fig. 7).

ramp filter, $|\nu|$, with a smooth function. We choose the Hann filter defined by :

$$H(\nu) = \begin{cases} 0.5\left(1+\cos\left(\pi\frac{\nu}{\nu_{\max}}\right)\right) & \text{if} \quad |\nu| < \nu_{\max} \\ 0 & \text{if} \quad |\nu| \geq \nu_{\max} \end{cases} \tag{11}$$

where $\nu_{\max}$ is the maximum value of the frequency of the discretized projections. Thus the ramp filter becomes $H(\nu)|\nu|$. Other choices of the windowing function H are of course possible. These are examples of standard filters which are smoother and smoother: Ram-Lak, Shepp-Logan, Cosine, Hamming, Hann, Blackman; see Fig. 9 for the associated ramp filters and see Fig. 10 for their spatial counterparts. Changing the filter changes the artifacts of reconstruction: increasing the Fourier-smoothness of a window decreases its maximum spatial-amplitude, produces weakest oscillations of the tail, and thus increases stability. For instance, the Ram-Lak window produces a Gibbs phenomenon due to the strong jump of the Fourier-window: overshoot, undershoot and ringing. The Hann filter window that has been chosen for this paper presents the advantage of being continuous; then the spatial-filter decreases faster to zero and the filtering is less sensitive to noise.

Fig. 11 displays the reconstruction of the contours using the FBP algorithm on reflection data from Fig. 6. The FBP algorithm has also been applied on the suppport set from Fig. 8, see Fig. 12. The convex part of the contours is recovered in both reconstructions. Furthermore the upper left part of the object, which is non-convex, is reconstructed only in the first case: FBP on

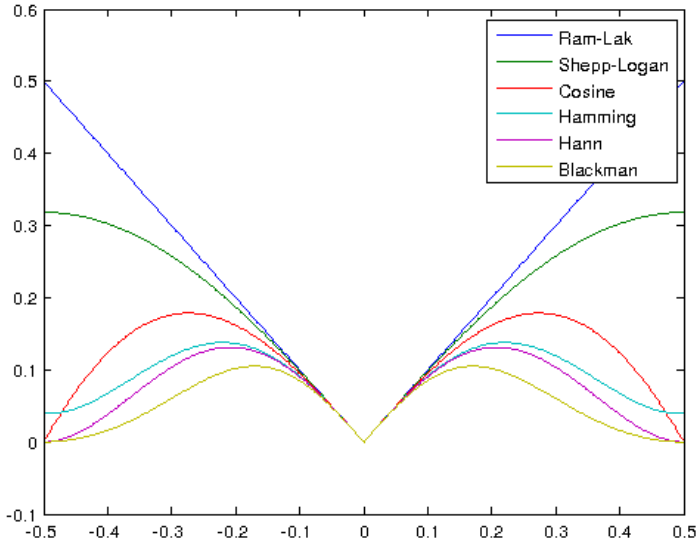

Figure 9: Smoother and smoother ramp filters in the (ν-)frequential domain.

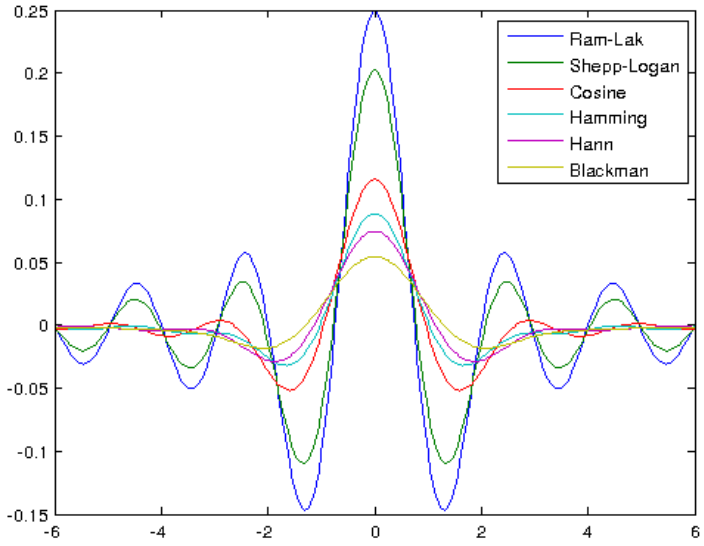

Figure 10: Representation of the filters of Fig. 9 in the (p-)spatial domain.

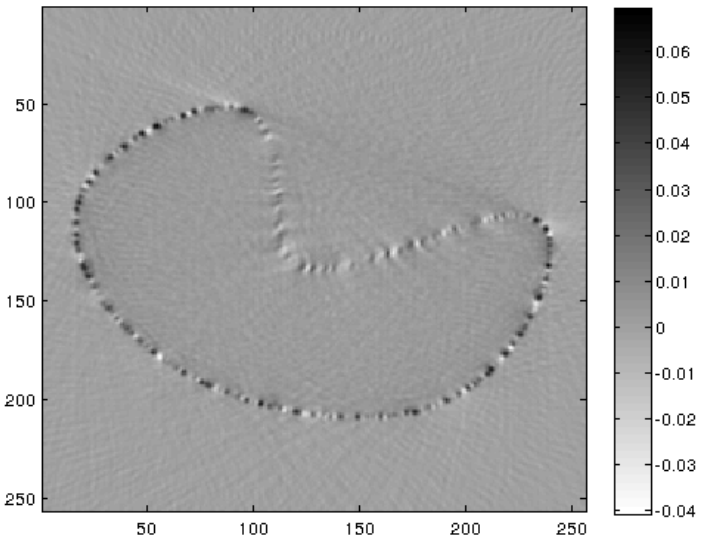

Figure 11: FBP reconstruction with the reflection data from Fig. 6

varying reflection data is richer than FBP on shapes. Artifacts can be observed in both cases. They are due to the incompleteness: the point spread function (cosine function for the classical Radon transform) are incomplete.

To complete the numerical study, we consider the same object, with a smoothly varying function f: see Fig. 13. Data and reconstruction are depicted in Figs. 14 and 15. Again, the object is reconstructed with incompleteness artifacts.

4 Applications to laser imaging

We present now the extension of Computerized Tomography to 3D Laser Imagery. More particularly, we illustrate the method with real data.

4.1 Principle

We assume that a laser source turns around a 3D scene. The scene may contain an object with or without occultations. At each position, the laser illuminates the scene, and a receptor array measures the backscattered light in a focal plane, in the monostatic configuration. Thus we get a set of 2D images; it contains backscattered intensities, resulting from an interaction of the laser beam with surfaces of the scene. The aim is to reconstruct the 3D scene from these 2D images.

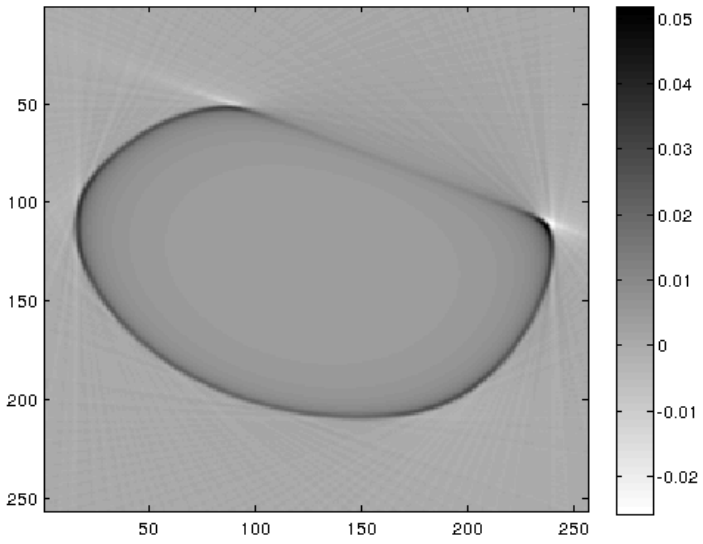

Figure 12: FBP reconstruction with the support from Fig. 8

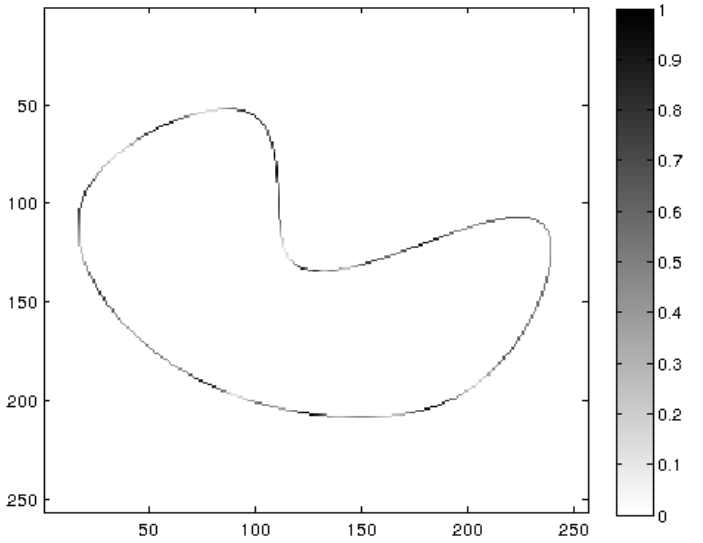

Figure 13: Original synthetic contours, with a smooth function

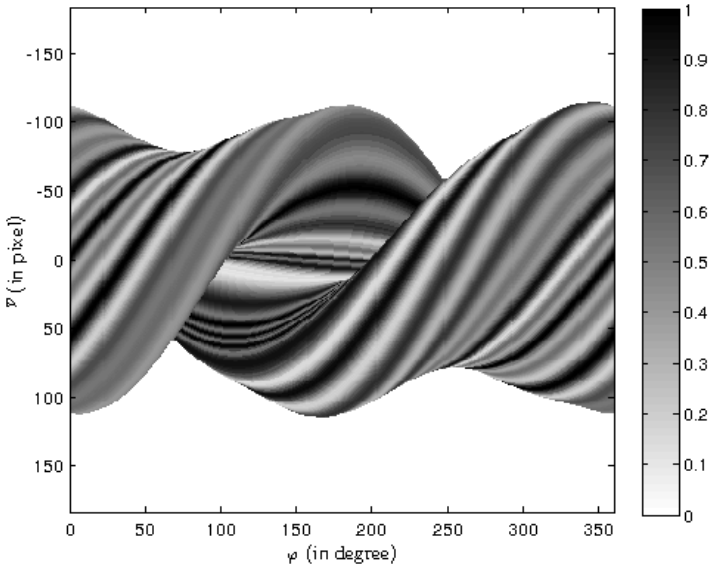

Figure 14: Reflection data from Fig. 13.

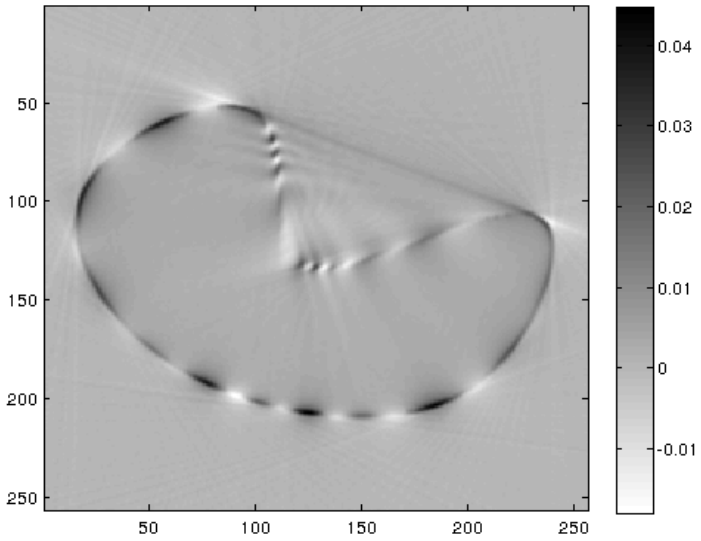

Figure 15: FBP reconstruction from Fig. 14

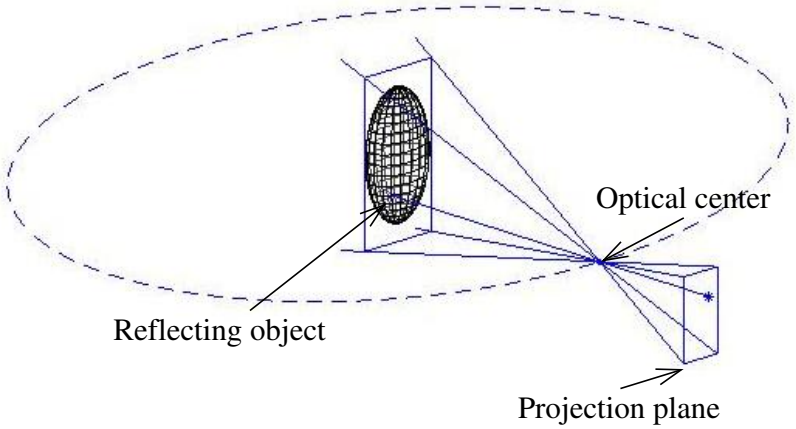

Figure 16: Perpective projection through a pinhole camera

In the sequel we consider that a laser image is designed according to an optical model, such as perspective projection through a pinhole camera; see Fig. 16. After a laser illumination each object point of the scene reemits in many directions. An optical instrument is used to record the data. It contains a receptor plane which is (parallel to) the tangent plane of the circle, and it is assumed to refocused rays coming from a same object point to a same image point in the receptor plane; this image point is aligned with some optical center of the recording instrument and the object point. As a result a laser image is a projection of the scene along rays through the optical center. So the acquisition geometry is exactly a cone-beam scanning geometry as the transmission tomography one.

Then the laser signal is considered as a sinogram and is processed with a FBP-kind algorithm: the FDK algorithm is used as a heuristic to compute fastly a 3D volume of the scene. Eventually (but not necessary), when the acquisition device is in far field with respect to the scene, the acquisition geometry tends to a parallel geometry and processings can be reduced to parallel FBPs, 2D slice by 2D slice.

4.2 Simulation results

In this part, we present the results obtained applying a FBP algorithm on realistic data (courtesy of Thales Optronics). The computations are performed on a GPU: Nvidia Tesla C2075. This enables short computation times.

The first case deals with real laser data. A car is illuminated with the laser imaging system that has been presented above. In the reconstruction process, the sought volume is discretized on a 127x127x342 grid. The measurements are defined on a 360x181x342 grid. The contrasts are first adjusted by a rescaling: data are here pre-processed with a (12-th) root. Slices of the resulting real 3D

laser sinogram are depicted in Fig. 17; the vertical slice is one laser image of the sequence, and the horizontal slice looks like a 2D fan-beam sinogram. We can observe a noise which is due to the scintillation phenomenona. The FBP of these real data is performed here in 2.3 seconds. Fig. 18 shows the 3D reconstruction of the car. This visualization of the reconstructed volume has been obtained with the isovolume functionnality of the free software ParaView [24], with a lower threshold of 10%. The features of the car are well-reconstructed; some details such as door handle are also reconstructed.

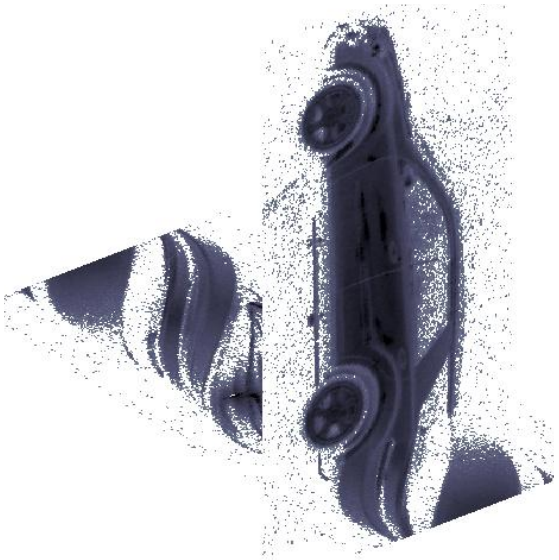

Figure 17: Slices through a real laser sinogram.

In a second time, the method is tested on a simulated complex 3D scene which is discretized on a 179x179x229 grid. Now the car is partially occluded by trees. The size of the data is 360x254x229. As before, slices are depicted by Fig. 19 after rescaling. The reconstruction is shown in Fig. 20, with a threshold of 10%. The computation time for this example is about 2.5 seconds. The car and the trees (including the foliage) are both reconstructed. Lacunarities are due to the occultations and thresholding.

5 Conclusion

We have seen in this work how the connection between the considered reflection modality and the classical transmission modalities (CT-scan) could encourage the use of fast and accurate algorithms such as FBP to recover a 3D scene from a set of 2D images. The lambertian diffusion was first considered and appears to be consistent in terms of support with the classical sinogram (Radon transform). Then, we have considered laser sinograms from 3D complex scenes. The

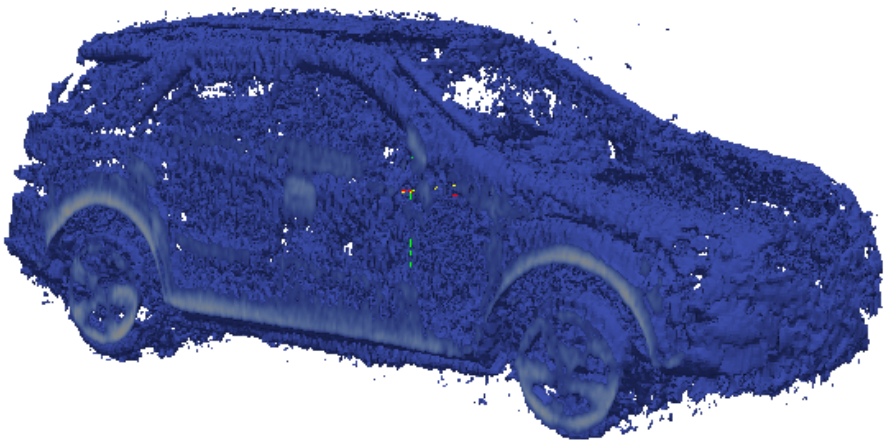

Figure 18: Reconstruction using FBP on data shown in Fig. 17

application of the FDK algorithm on them provides fastly 3D reconstructions that can be used for identification.

Acknowledgement

This work has been partially supported by the *DatDriv3D+* project, which is sponsored by the French Ministry of Economy: Directorate General of Competitiveness, Industry and Services; this project is part of program RAPID implemented by French Directorate General of Armament.

References

[1] F. Knight, S. Kulkarni, R. Marino, and J. Parker, *Tomographic Techniques Applied to Laser Radar Reflective Measurements*. Lincoln Laboratory Journal, 2(2), 1989.

[2] J. Sharpe, *Optical projection tomography as a new tool for studying embryo anatomy*. Journal of anatomy, 202(2):175-181, 2003.

[3] L. Feldkamp, L. Davis and J. Kress, *Practical cone-beam algorithm*. JOSA, 1(6):612-619, 1984.

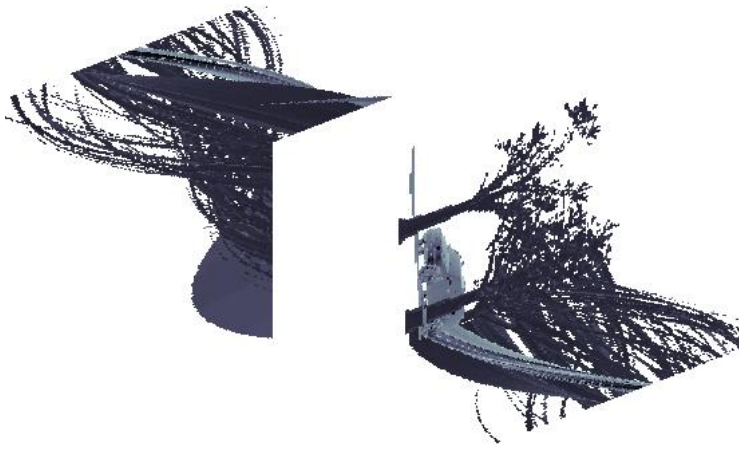

Figure 19: Slices through a simulated laser sinogram.

[4] G. Berginc and M. Jouffroy, *Optronic system and method dedicated to identification for formulating three-dimensional images*, US patent 20110254924 A1, European patent 2333481 A1, FR 09 05720 B1, November 2009.

[5] G. Berginc and M. Jouffroy, *Simulation of 3D laser systems*. In Geosciences and Remote Sensing Symposium, 2009 IEEE International, IGARSS 2009, vol. 2, pp 440-444, 2009.

[6] G. Berginc and M. Jouffroy, *Simulation of 3D laser imaging*. PIERS Online, 6(5):415-419, 2010.

[7] G. Berginc and M. Jouffroy, *3D laser imaging*. PIERS Online, 7(5):411-415, 2011.

[8] G. Berginc, *Scattering models for range profiling and 2D-3D laser imagery*. In Hanssen, L. M., editor, *Reflection, Scattering, and Diffraction from Surfaces IV, 92050K*, volume 9205 of *Proc. of SPIE*, 2014.

[9] F. Natterer and F. Wübbeling, *Mathematical methods in image reconstruction*. SIAM, 2007.

[10] H.P. Hiriyannaiah, *X-ray computed tomography for medical imaging*. Signal Processing Magazine, IEEE, 14(2), pp 42-59, 1997.

[11] H. Miao, *Implementation of FDK Reconstruction Algorithm in Cone-Beam CT Based on the 3D Shepp-Logan Model*. Biomedical Engineering and Informatics, 2009. BMEI '09. 2nd International Conference, pp 1-5, doi: 10.1109/BMEI.2009.5304987, 2009.

[12] P. Grangeat, *Analyse d'un système d'imagerie 3D par reconstruction à partir de radiographies X en géométrie conique*. Ph.D. thesis, Ecole Nationale Supérieure des Télécommunications, 1987.

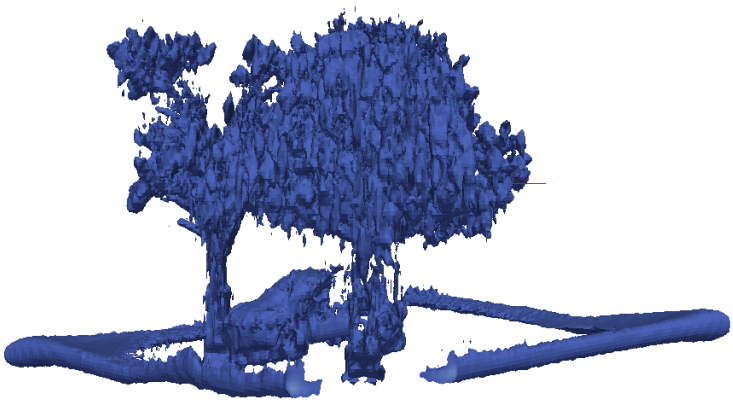

Figure 20: Reconstruction using FBP on data shown in Fig. 19

[13] M. Defrise and R. Clack, *Filtered backprojection reconstruction of combined parallel beam and cone beam SPECT data*. Phys. Med. Biol. 40 1517 doi:10.1088/0031-9155/40/9/010, 1995.

[14] M. Sakamoto, H. Nishiyama, H. Satoh, S. Shimizu, T. Sanuki, K. Kamijoh, A. Wattanabe and A. Ashara, *An implementation of the Feldkamp algorithm for medical imaging on cell* . IBM Corporation Systems and Technology Group, 2005.

[15] A.G. Voronovich, *Small-slope approximation for electromagnetic wave scattering at a rough interface of two dielectric half-spaces waves*. Random Media 4, pp 337-367, 1994.

[16] G. Berginc, *Small-slope approximation method: a further study of vector wave scattering from twodimensional surfaces and comparison with experimental data*. Progress in Electromagnetics Research, PIER 37, Zhang Y. and Grzegorczyk T.M. (Ed.), EMW Publishing, Cambridge, USA, 251-287, 2002.

[17] G. Berginc and C. Bourrely, *The small-slope approximation method applied to a three-dimensional slab with rough boundaries*. Progress In Electromagnetics Research, PIER 73, J. A. Kong (Ed.), EMW Publishing Cambridge, USA, 131-211, 2007.

[18] L.M. Pedrotti and L.S. Pedrotti, *Introduction to Optics*. Prentice Hall. ISBN 0135015456,1993.

[19] P. Beckmann and A. Spizzichino, *The scattering of electromagnetic waves from rough surfaces*. Pergamon Press, 1963.

[20] G. Berginc and A.A. Maradudin, *Scattering properties of random structures in thin films*, in [Optical thin films and coatings], A Piegari and F. Flory (Ed.), Woodhead Publishing Limited, Oxford, 177-289, 2013.

[21] J.H. Lambert, *Photometria*. sive de Mensura et gradibus luminis, colorum et umbrae, 1760.

[22] E.T. Quinto, *Tomographic reconstructions from incomplete data-numerical inversion of the exterior Radon transform*, Inverse Problems, 4, 867, 1988.

[23] J. Boman and E.T. Quinto, *Support theorems for real-analytic Radon transforms*. Duke Math. J. Volume 55, Number 4 (1987), 943-948.

[24] A. Henderson, J. Ahrens, and C. Law, *The ParaView Guide*, Kitware Inc., 2004, Clifton Park, NY.